Hindawi
Indoor Air
Volume 2024, Article ID 9927275, 18 pages
https://doi.org/10.1155/2024/9927275

Research Article

A Direct Infection Risk Model for CFD Predictions and Its Application to SARS-CoV-2 Aircraft Cabin Transmission

Florian Webner[1], **Andrei Shishkin**[1], **Daniel Schmeling**[1] and **Claus Wagner**[1,2]

[1]*Institute of Aerodynamics and Flow Technology, German Aerospace Center (DLR), 37073 Göttingen, Germany*
[2]*Institute of Thermodynamics and Fluid Mechanics, TU Ilmenau, 98693 Ilmenau, Germany*

Correspondence should be addressed to Florian Webner; florian.webner@dlr.de

Received 11 July 2023; Revised 15 December 2023; Accepted 2 January 2024; Published 25 January 2024

Academic Editor: Geun Young Yun

Copyright © 2024 Florian Webner et al. This is an open access article distributed under the Creative Commons Attribution License, which permits unrestricted use, distribution, and reproduction in any medium, provided the original work is properly cited.

Current models to determine the risk of airborne disease infection are typically based on a backward quantification of observed infections, leading to uncertainties, e.g., due to the lack of knowledge whether the index person was a superspreader. In contrast, the present work presents a forward infection risk model that calculates the inhaled dose of infectious virus based on the virus emission rate of an emitter and a prediction of Lagrangian particle trajectories using CFD, taking both the residence time of individual particles and the biodegradation rate into account. The estimation of the dose-response is then based on data from human challenge studies. Considering the available data for SARS-CoV-2 from the literature, it is shown that the model can be used to estimate the risk of infection with SARS-CoV-2 in the cabin of a Do728 single-aisle aircraft. However, the virus emission rate during normal breathing varies between different studies and also by about two orders of magnitude within one and the same study. A sensitivity analysis shows that the uncertainty in the input parameters leads to uncertainty in the prediction of the infection risk, which is between 0 and 12 infections among 70 passengers. This highlights the importance and challenges in terms of superspreaders for risk prediction, which are difficult to capture using standard backward calculations. Further, biological inactivation was found to have no significant impact on the risk of infection for SARS-CoV-2 in the considered aircraft cabin.

1. Introduction

Numerous pandemics have occurred in the past. Examples include the pandemics caused by the infection with SARS-CoV-1 in 2002/03, the H1N1 swine flu virus in 2009/10, and most recently SARS-CoV-2. With regard to the latter, it is well known from many observations during the COVID-19 pandemic that the majority of infections occurred by airborne transmission of SARS-CoV-2 [1] indoors rather than outdoors [2]. Therefore, the ventilation of indoor spaces or cabins and compartments of various public transportation vehicles (e.g., buses, passenger trains, and airplanes) is of particular concern as the passengers sit close together. In order to compare the infection risk of pandemic or endemic diseases (influenza, SARS-CoV-2) at different locations (e.g., train vs. supermarket) or countermeasures at the same location (e.g., the ventilation concept), absolute risk assessment capabilities must be established. In addition, an improved understanding of infectious disease transmission is essential to determine and, if necessary, minimize the risk of infection for the passengers and the crew on trains and airplanes during future waves of airborne diseases. The studies conducted for this purpose must take into account a variety of influences: on the one hand, the number and size of virus-carrying aerosol droplets emitted by an infected person, as well as their transport pathways and residence times in partially air-conditioned or ventilated enclosed spaces, must be predicted and measured. On the other hand, the viruses inhaled by other people and their infectivity must be determined for each person. All of this can only be achieved with sufficient reliability through a clever combination and mutual validation of observations, measurements, and numerical simulations.

In 1955, Wells [3] proposed the idea that pathogens are exhaled and inhaled in discrete quantities. He defined a

quantum as the dose sufficient to cause disease in approximately 63% of the exposed individuals. Riley et al. [4] determined a quantum emission rate of 1.5 quanta/s based on the number of detected infections during an outbreak of measles in a school in 1974. They assumed that the air in the rooms was well mixed so that the pathogens were homogeneously distributed throughout the room immediately after emission. This approach became known as the "Wells-Riley" model. Most studies predicting the risk of infection are based on determining the above-mentioned quantum by backward calculation [5–7]. The Wells-Riley model has also been used in several studies to estimate the risk of SARS-CoV-2 infection. For example, Sun and Zhai [8] used it to infer a quantum emission rate of 0.238 quanta/s from a detected transmission on a bus in Hunan, China, based on the number of ill individuals. In addition, Buonanno et al. [9] used a derived method to estimate the quantum emission rate for SARS-CoV-2 infections by substituting unknown values for SARS-CoV-2 infections—such as the number of RNA copies emitted and quanta per RNA—with known values for SARS-CoV-1 infections, resulting in quantum emission rates ranging from less than 1 quantum/h to more than 100 quanta/h.

Since the introduction of the well-mixed room assumption by Riley in the 1980s, computing power has increased significantly. Moreover, passenger comfort and air quality have become more important in all modes of transportation. As a result, many model-based computational fluid dynamic (CFD) simulations have been performed over the recent years to study the ventilation of various modes of public transportation—including buses, trains, and airplanes—with the goal of evaluating and, if necessary, improving thermal comfort and air quality. Specially designed measurements have also been performed to validate the computational fluid dynamic (CFD) methods used for this purpose. For example, Zhang et al. [10] replicated the aerosol dispersion from an infected passenger in a city bus in a laboratory experiment and demonstrated that opening doors and windows reduced the concentration of pollutants in the city bus by about half. Other approaches focused on ventilation in trains, such as the CFD study by Konstantinov and Wagner [11] and the experimental study by Schmeling et al. [12]. In addition, Shinohara et al. [13] performed measurements in a naturally ventilated commuter train to estimate the air change rates and to assess the infection risk using CO_2 decay methods. Their measurements show a strong correlation between the air exchange rates and the train speed. They also observed a significant reduction (91% to 94%) in the modeled infection risk at high speeds and with open windows. Woodward et al. [14] performed CO_2 and aerosol measurements in a train car as well as flow visualizations using artificial fog and found that the flow patterns in the cross section of the car were strongly influenced by the ventilation system and differed considerably between the center and the end of the car. Similar studies focusing on aerosol transport have also been conducted for the aircraft cabin. For example, Gupta et al. [15] calculated cough-induced aerosol transport in an aircraft cabin as part of transient CFD simulations using the commercial fluid simulation software Fluent. Later, Gupta et al. [7] used CFD-predicted particle dispersion to determine the risk of infection with the influenza virus based on posterior quantum estimation and to evaluate the effect of N95 masks. You et al. [16] utilized CFD to predict contaminant transport and back-calculate the quantum emission rate of a SARS-CoV-1 superspreading event in a Boeing 737 aircraft cabin resulting in 11 secondary infections, where exact seat locations of the index person and infected subjects are known. However, the quantum emission rate is usually determined based on the well-mixed room assumption by Riley et al. [4] as the boundary conditions at the time of infection are usually not known with sufficient accuracy. Therefore, a disadvantage of this posterior quantum estimation is that the predicted risk is often independent of the detailed particle transport. Furthermore, the quantum dose often represents an outstanding event that led to many infections, e.g., as observed in the study conducted by You et al. This can give superspreader events a higher weight than normal infections, which in turn has a negative impact on the accuracy of infection risk prediction. For example, Mikszewski et al. [17] showed that the rate of quantum emission varied between 15 and 4214 quanta/h based on 16 events reported in 6 studies. Despite this large scatter, there are now a number of numerical studies that use the backward quantum estimation. One example is the work of Wang et al. [5], who investigated the SARS-CoV-2 infection risk in Chinese passenger trains. Their study is based on CFD simulations using a quantum emission rate of 14 quanta/h obtained by Dai and Zhao [18], who fitted quantum emission rates and reproduction numbers for different infectious diseases. For validation, Wang et al. had access to a unique dataset of 2334 Chinese train rides with at least one SARS-CoV-2-positive person, resulting in 234 secondary infections. Details on the seat positions of the index and secondary cases were also available. These data were collected as part of China's COVID-19 testing strategy and published by Hu et al. [19]. In addition to the shortcomings of the backward quantum estimation, Pourfattah et al. [20] reviewed infection risk models and observed that biological inactivation of the pathogens is often neglected, which leads to inaccurate risk prediction.

Therefore, rather than relying on posterior estimation of quantum emissions or using other indirect methods, the focus of the present work is the development of an infection risk model based on measured data from infected humans. Although human challenge studies are ethically problematic, they have been performed for several pathogens [21–23] including SARS-CoV-2 [24]. Furthermore, even though the required human challenge studies raise ethical issues, they also provide controlled data on the inoculation dose and the corresponding infection rate (among participants) and thus the dose-response relationship. To calculate the inhaled dose, the amount of exhaled infectious virions is required, which is determined based on the typical distributions of the number and size of aerosol droplets generated during human respiratory events, as summarized by Pöhlker et al. (preprint) [25] and the virion distribution as a function of aerosol particle size given by, e.g., Alsved et al. [26] for SARS-CoV-2. However, the viral load of the aerosol droplets as a function of the diameter is difficult to determine and

rarely available. This has led researchers to assume that the virus concentration (measured in RNA copies/ml) in the aerosol particles is comparable to the virus concentration in the throat or nose [27, 28]. That this assumption is not always true was shown by Lai et al. [29], who compared the viral load in aerosol exhaled during breathing and coughing by individuals infected with SARS-CoV-2. They showed that virus emission during coughing was raised by increasing the viral load on the "smaller" aerosol particles ($<5\,\mu$m) but not on the "larger" particles ($>5\,\mu$m), even though most of the exhaled particle volume was present as "larger" particles [25]. This observation supports that the size of aerosol particles depends on the site of their formation in the respiratory tract (smaller particles are formed in the deeper airways) and that viruses primarily colonize certain sections of the respiratory tract. Consequently, the viral concentration of aerosol particles is high when they are formed at the site of infection. In addition, this is supported by observations by Alsved et al. [26] who determined the SARS-CoV-2 virus concentration by examining exhaled aerosol particles from infected individuals by distinguishing 8 different particle size bins from 0.14 μm to 8 μm and found a maximum virus concentration in the 1.7-2.8 μm particle size bin (for singing) and only one-fifth of the concentration for the 2.8-4.5 μm particle size bin.

The model presented below requires pathogen-specific parameters. After introducing the model, we apply it to predict the risk of SARS-CoV-2 infection in an aircraft cabin using the aerosol RNA emission, e.g., determined by Malik et al. [30] and Li et al. [31], the proportion of infectious units per RNA presented by Sender et al. [32], and the biological inactivation of SARS-CoV-2 determined by Dabisch et al. [33]. All in all, a model-based prediction of the probability of infection can be realized with additional consideration of the dose-response model derived from the human challenge study performed by Killingley et al. [24]. Furthermore, the particle transport in the cabin of the Do728 aircraft is calculated by CFD using a method that has been validated in the past by comparison with measurements (see Schmeling et al. [34]). Accurate knowledge of particle trajectories and sizes is important for realistic model predictions of the particle deposition on surfaces, particle flight time as a function of size, and biological inactivation of viruses. Furthermore, the sensitivity of the input parameters (i) biological inactivation rate, (ii) number of exhaled viruses, (iii) infectious units per RNA, and (iv) flight or exposure time to the risk of SARS-CoV-2 infection in the Do728 aircraft cabin is discussed at the end of the paper.

2. The Infection Risk Model

The risk of infection is modeled in two main steps:

(1) The inhalation rate of the infectious dose $\dot{D}_{\text{in}}$ is determined by means of the exhalation, transport, and the inhalation processes shown in Figure 1 and discussed in Sections 2.1 to 2.3. Different cases are discussed in Section 2.4

(2) The risk of infection I is estimated based on the dose inhalation rate from the first step using a dose-response relationship (Section 2.5)

Figure 1 illustrates the process steps of virus transport: exhalation, transport, and inhalation. For exhalation, $\dot{R}$ (RNA/s) and $\dot{P}$ (1/s) describe the emission rates of virions and particles, respectively. f describes the fraction of infectious virions (TCID_{50}/RNA) at the time of exhalation. The virus stability $s(1)$ indicates how many of the infectious virions remain infectious during transport, and C_B describes the particle concentration in the breathing zone. Finally, the inhalation is represented by the pulmonary ventilation rate p_{in} (m^3/s). These parameters are explained in more detail below, assuming that the pathogen is an RNA virus, although it could be a DNA virus, a bacterium, or a fungus. Therefore, the pathogen load is given in units of RNA (copies), and the infectious dose is expressed in units of 50% tissue culture infectious dose (TCID_{50}).

2.1. Exhalation. The exhalation process includes determining the virus and/or particle emission rate and the infectious RNA fraction, as described below.

2.1.1. Virus and Particle Emission Rate: $\dot{R}_j, \dot{P}_j$. During human exhalation, particles of different sizes are exhaled in a multimodal particle size distribution (PSD) [25]. The size of the particles is assumed to depend on the formation mechanism and therefore the site of formation in the respiratory tract. In general, smaller particles are formed deeper down in the alveolar region of the lung and the largest particles are formed in the upper respiratory tract, i.e., in the mouth and nose. In addition, the pathogens may infect certain areas of the respiratory tract more severely than others or may be cleared more rapidly from certain regions of the respiratory tract. Since the virus concentration of the respiratory liquid may vary along the respiratory tract, the virus concentration v (RNA/ml) of the aerosol liquid depends on the site of formation. Further, since the particle size indicates the site of formation in the respiratory tract, it also indicates the virus concentration of the aerosol particles. Therefore, the virus emission rate for the j^{th} diameter range $\dot{R}_j$ depends on the mean virus concentration v_j, the mean particle volume V_j (m^3), and the mean number of particles emitted by a human per second $\dot{P}_j^h$ (1/s) for the j^{th} particle size bin, respectively:

$$\dot{R}_j \approx v_j V_j \dot{P}_j^h. \tag{1}$$

Multiplying v_j by V_j gives the number of virions per particle for the j^{th} size bin. Further, multiplication by the human particle emission rate gives the corresponding pathogen emission rate.

In equation (1), the virus concentration in the aerosol liquid v_j is a necessary parameter which can be taken from Alsved et al. [26], who measured v in eight size bins based on a single participant. Alternatively, the virus concentration

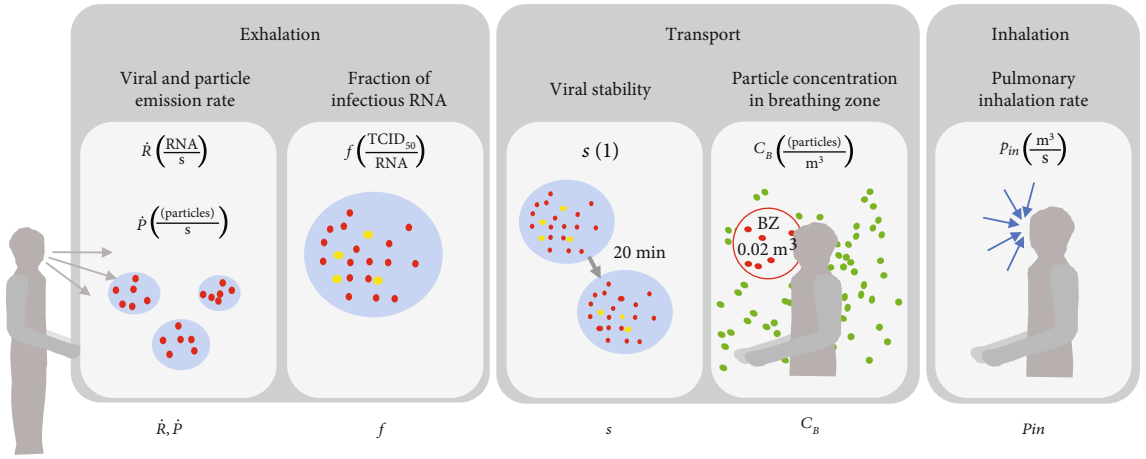

FIGURE 1: Process steps and terms for the calculation of the inhalation rate of the infectious dose $\dot{D}_{\text{in}}$.

from nasal or throat swabs could be used instead as for example done by Henriques et al. [35]. However, as described above, this value may differ from the actual v at the site of particle generation. Studies have shown that there is little or no correlation between the virus concentration in exhaled particles and the virus concentration in the upper respiratory tract (URT) [30]. Moreover, the risk of transmission is more strongly correlated with virus emission via exhaled particles than with virus concentration in the URT [36]. Thus, we avoid using the viral load of the URT. In addition, when using the latter approach, evaporation must be taken into account, as it significantly reduces the particle volume [27, 37] (depending on the ambient humidity and composition of the mucosal fluid), resulting in a higher virus concentration in the particle.

The volume of the aerosol particles can be approximated by $V = \pi D^3/6$, assuming that the particles are of spherical shape. Again, data from the literature are required to estimate the number of aerosol particles emitted per second by human exhalation for different size bins $\dot{P}_j^h$, as for example provided by Pöhlker et al. [25].

Several studies [29, 38] measure the virus emission rate $\dot{R}$ from humans directly. However, these studies typically do not distinguish between different particle sizes and are therefore not suitable to determine $\dot{R}_j$.

2.1.2. Fraction of Infectious RNA Copies f. Not all copies of the virus are infectious [32]. The receptors of the virus or the RNA itself may be damaged, thus preventing the virus from infecting cells or replicating. Therefore, it is necessary to determine the number of infectious virus copies among all virions. In the case of living pathogens—such as bacteria—this would be equivalent to the fraction of living bacteria to all bacteria. f would ideally be measured in the aerosol immediately after exhalation. However, data are scarce so the value in respiratory tissue must be used in the absence of better data.

2.2. Particle Transport. As mentioned above, particle transport is commonly circumvented by assuming that particles are perfectly homogeneously distributed in space immediately after emission, the so-called well-mixed room assumption. In contrast, we use information about the velocity and turbulent kinetic energy in the flow field to predict the Lagrangian transport of individual particles (see Section 3.1). Since the virus copies are inactivated over time while being suspended in the air, the duration of the transport is relevant to estimate the virus inactivation. The particle concentration in the breathing zones and the virus stability are discussed in more detail below.

2.2.1. Fraction of Particles Reaching the Breathing Zone B_j. The breathing zone (BZ) is defined near the target's face (we use a hemispherical shape with the center at the nose, similar to [39]). Then, the number of particles in the j^{th} size bin $N_{B,j}$ [1] in the BZ is divided by the volume of the BZ V_B (m^3) to obtain $C_{B,j}$ (1/μm^3):

$$C_{B,j} = \frac{N_{B,j}}{V_B}. \tag{2}$$

With equation (2), B_j can be calculated:

$$B_j = \frac{C_{B,j}}{\dot{P}_j} = \frac{N_{B,j}}{V_B \dot{P}_j}. \tag{3}$$

For a steady $\dot{P}_j$, the number of particles of the j^{th} size bin in the BZ $N_{B,j}$ is proportional to the particle emission rate of this size bin $\dot{P}_j$ (particles have to be counted to their initial size bin, even after evaporation). This assumption would be violated if the particles were interacting, but according to [40], the number of particles is too small to allow for interaction. Therefore, B_j is constant for any particle emission rate, so that $\dot{P}_j$ can be chosen freely ($\dot{P}_j$ must be greater than zero, otherwise equation (3) is not defined).

2.2.2. Virus Stability s. Virus stability describes the resistance of a virus to inactivation. The loss rate $\dot{d}$ depends on the pathogen/strain and on environmental factors, such as UV

radiation, temperature, and humidity [33]. To determine the biological inactivation, it is necessary to consider both the loss rate (%/min) of the pathogen of interest and the travel time τ_i required for the i^{th} particle to reach the BZ. The mean stability s in the BZ is obtained by calculating the probability of inactivation for each pathogen copy and then averaging the results:

$$s = \frac{1}{n}\sum_{i=1}^{n}\left(1-\dot{d}\right)^{\tau_i/T_0}. \tag{4}$$

Here, n is the number of CFD particles in the BZ, $\dot{d}(1)$ is the fraction of virions being inactivated during T_0 (s), and τ_i (s) is the residence/travel time of the i^{th} particle at the time of inhalation.

2.3. Inhalation p_{in}. The particle concentration for the j^{th} size bin in the BZ $C_{B,j}$ is described above. The pulmonary inhalation rate p_{in} (m^3/s) can be used to calculate the inhalation rate of particles for the j^{th} size bin (the exact deposition site in the respiratory tract is neglected, further discussion in Section 2.5). Based on the literature, typical inhalation rates for passengers at rest are 6 l/min (or $10^{-4}\,\text{m}^3$/s) [41].

2.4. Case Distinction for the Inhalation Rate of the Infectious Dose $\dot{D}_{in}$. First, we consider $\dot{D}_{\text{in}}$ by making useful assumptions, i.e., a steady-state and size-independent particle transport. Then, we take the particle size into account and finally consider an unsteady case.

2.4.1. Steady-State and Size-Independent Particle Transport. Bivolarova et al. [42] showed experimentally that there is no significant difference in the distribution between particles with diameters of 0.7 μm and 3.5 μm. Therefore, under certain circumstances, the particle transport can be assumed to be independent of the particle size. With this assumption, the inhalation rate of the infectious dose $\dot{D}_{\text{in}}$ is given in TCID_{50}/s:

$$\dot{D}_{\text{in}} = \dot{R} f s B p_{\text{in}}, \tag{5}$$

$$D_{\text{in}} = \dot{D}_{\text{in}} t_x, \tag{6}$$

where the meaning of the parameters in equation (5) is similar to those described in Sections 2.1 to 2.3, but for all diameters instead of a specific bin size. Hence, the subscript j, indicating the j^{th} size bin is omitted. Thus, the model depends only on the fraction of particles reaching the BZ, not their absolute number, size, or viral load. For example, if 3% of emitted particles reach the BZ, then 3% of RNA copies reach the BZ independently of the size or viral load of the particles. However, this assumption only holds true if the particle transport is independent of the particle size.

In a steady state, $\dot{D}_{\text{in}}$ is constant and can be multiplied by the exposure time t_x to obtain the total inhaled infectious dose D_{in} (TCID_{50}) (equation (6)).

As mentioned above, in a steady state, the number of particles in the BZ C_B is proportional to the particle emission rate $\dot{P}$. Therefore, $C_B/\dot{P}$ is a constant, which we call B. Using a realistic human particle emission rate poses two problems: on the one hand, there is a significant person-to-person variation in particle emission rates, which causes uncertainty. On the other hand, particle emission of humans may be low (in total or for certain diameters), creating statistical uncertainty. Since equation (5) is independent of $\dot{P}$, any particle emission rate can be used.

Substituting equations (3) and (4) into equation (5) gives

$$\dot{D}_{\text{in}} = \dot{R} f \left(\frac{1}{n}\sum_{i=1}^{n}\left(1-\dot{d}\right)^{\tau_i/T_0}\right)\frac{C_B}{\dot{P}} p_{\text{in}}, \tag{7}$$

where all parameters are available from the literature or CFD results.

2.4.2. Steady PSD and Size-Dependent Particle Transport. Particle size must be considered, for example, when comparing particles with ballistic trajectories (dominated by gravity and inertia) to particles, where the drag force is dominant. By considering m different ranges of particle diameters, equation (7) can be solved separately for each diameter range. For this, $\dot{R}$ must be replaced by $\dot{R}_j$ in accordance with equation (1). The sum of the infectious dose inhalation rates of all diameters results in the total $\dot{D}_{\text{in}}$:

$$\dot{D}_{\text{in}} = \sum_{j=1}^{m} v_j V_j \dot{P}_j^h f \left(\frac{1}{n}\sum_{i=1}^{n}\left(1-\dot{d}\right)^{\tau_i/T_0}\right)\frac{C_{B,j}}{\dot{P}_j} p_{\text{in}}, \tag{8}$$

where the subscript j denotes the j^{th} diameter range (size bin) for v, V, $\dot{P}^h$, $\dot{P}$, and C_B, which then applies to size-dependent particle transport.

2.4.3. Unsteady Virus Emission and Size-Dependent Particle Transport. While COVID-19 is commonly transmitted by asymptomatic individuals via normal breathing or talking, other diseases may be transmitted primarily by coughing or sneezing. Breathing and talking can be approximated by a steady virus emission rate $\dot{R}$, but coughing and sneezing are highly unsteady. Therefore, $\dot{D}_{\text{in}}$ (from equation (8)) must be integrated over time to model unsteady virus emission rates:

$$\dot{D}_{\text{in}} = \sum_{j=1}^{m}\int_{t_0}^{t_1} v_j(t) V_j \dot{P}_j^h(t) f \left(\frac{1}{n}\sum_{i=1}^{n}\left(1-\dot{d}\right)^{\tau_i/T_0}\right)\frac{C_{B,j}}{\dot{P}_j} p_{\text{in}}\,\mathrm{d}t, \tag{9}$$

where v_j and $\dot{P}_j^h$ are functions of time, while the other parameters are assumed to remain constant. We emphasize that the particle emission rate ($\dot{P}_j$) in the CFD can remain constant even during a coughing event, since only the fraction of released particles reaching the BZ is relevant, not the absolute number of particles. In contrast, $\dot{P}_j^h$ (the realistic particle emission rate of a human) is time-dependent to

calculate the amount of virions released (see equation (1)). A limitation of equation (9) is that it assumes that the susceptible person does not move until all emitted particles are removed from the room by deposition or ventilation.

2.5. Risk of Infection with Dose-Response Based on Human Challenge Data. The Wells-Riley model is based on the assumption that each inoculated pathogen has a certain chance to infect the host and that all hosts are equally susceptible. The risk of infection is then

$$I(D_{\text{in}}) = V(1 - \exp\,(k_h D_{\text{in}})), \tag{10}$$

where D_{in} (TCID_{50}) is the inhaled infectious dose, in this context V is the vulnerability of the susceptible individual ranging from zero to one, and k_h ($1/\text{TCID}_{50}$) is a fitting parameter representing the infectivity of the virion. V depends on the immunity, e.g., through previous infections or vaccines. A value of 1 indicates the highest level of vulnerability, whereas a value of 0 indicates 0% risk of infection due to total immunity.

The parameter k_h can be obtained from the results of a human challenge study with n_h participants of which m_h fall sick after inoculation with dose D_h:

$$k_h = \frac{\ln\,(1 - (m_h/n_h))}{D_h}. \tag{11}$$

2.6. Reference Case for SARS-CoV-2. The risk of infection depends on many parameters, some of which cannot be accurately predicted due to high variability from person to person (e.g., virus emission rate). Therefore, we define a reference case with realistic parameters. After evaluating the results of the reference case, we perform a sensitivity analysis to estimate the outcome for other values. The values chosen for the reference case are shown in Table 1 and discussed below.

2.6.1. Particle Size. Alsved et al. [43] found SARS-CoV-2 RNA in seven samples of exhaled aerosol particles $< 4\,\mu$m but only in two samples with particles $> 4\,\mu$m indicating that SARS-CoV-2 is predominant in smaller particles. Among another 22 participants, Coleman et al. [44] detected 85.4% of the RNA in particles $< 5\,\mu$m. Lai et al. [29] found a 5-fold higher virus load in particles $< 5\,\mu$m compared to particles $> 5\,\mu$m. The studies above measured the particles immediately after exhalation, which means that the particle size could be further reduced by evaporation after the measurement. In contrast, Lednicky et al. [45] investigated air samples in a car of an infected person during a 15-minute drive with closed windows and found more than 97% of the RNA in particles $< 2.5\,\mu$m with the only viable virus in particles $< 0.5\,\mu$m. Santarpia et al. [46] collected aerosol samples from hospital ward air, and only those in particles $< 4\,\mu$m were culturable (confirming they were active). Since low numbers of pathogens reduce the likelihood of successful culture [47], the observation that only pathogens from small particles are viable could be either due to the fact there are fewer pathogens or because they are actually less infectious. Both explanations have the same implication that small particles are most relevant.

In summary, the vast majority of SARS-CoV-2 virions are found in particles $< 5\,\mu$m. Thus, a simplification of the infection risk model is possible, if all particles $< 5\,\mu$m behave similarly, which we investigate in Section 3.2.2. The simplification eliminates the virus concentration v_j from the equation and instead requires the total virus emission rate $\dot{R}$ (see equations (7) and (8)). For most pathogens including SARS-CoV-2, there is significantly more data available in the literature for $\dot{R}$ than for v_j.

2.6.2. Virus Emission $\dot{R}$. We consider virus emission from continuous activities, such as breathing or talking, which we assume to be steady state. The person-to-person variability in virus emission is substantial. For example, Zhou et al. [48] measured the SARS-CoV-2 emission of 18 participants and observed that two of them emitted 85% of the total RNA copies. The strongest emitter exhaled 66% of the total RNA despite a low particle volume emission.

Most studies do not find exhaled RNA in approximately 30 to 50% of infected COVID-19 patients (see Table 1) resulting in a 0% risk of infection for all other passengers. Outliers with exceptionally high emission rates (100 times the median) occur occasionally. Jacot et al. [49] analyzed 4172 SARS-CoV-2 positive nasopharyngeal swabs and found a median viral concentration of 5×10^6 RNA/ml. Ten percent of the swabs contained more than 5×10^8 RNA/ml (100 times the median), indicating that a small percentage of individuals could cause the majority of infections. However, as discussed above, the viral load in aerosol is not necessarily comparable to the nasopharyngeal viral load. Therefore, we cannot infer the probability distribution of exhaled RNA from the probability distribution of RNA in the URT. Nevertheless, this finding supports the large person-to-person variation and relevance of superspreaders.

Table 1 provides an overview of virus emission rates from the literature. The lowest and highest observed virus emission varies significantly within and between the individual studies. We choose a value of 5×10^2 RNA/s, which lies between the mean values of 4.6×10^1 RNA/s observed by Malik et al. [30] and 5.6×10^3 RNA/s observed by Li et al. [31]. Of note, the number of exhaled virions remains high over time after symptom onset, but the probability of exhaling any virions decreases [30, 43, 50].

2.6.3. Fraction of TCID_{50} per RNA f. This parameter is necessary since not all RNA copies are infectious/active. To determine the infectivity of viruses, they are cultured, typically on Vero E6 cells. This requires a large number of SARS-CoV-2 copies: Kriegel et al. [47] estimated that 10^6, 10^7, and 10^8 copies result in a 20%, 50%, and 75% culture probability, respectively. In addition, Zhou et al. [52] reported that it is possible to find active SARS-CoV-2 on dry surfaces with $>10^5$ copies.

Data on the TCID_{50}/RNA ratio in exhaled aerosol is sparse. Adenaiye et al. [53] cultured 141 aerosol samples on Vero E6 cells, of which 2 were culture positive. Lai

Table 1: Virus emission rate values from the literature.

Author	Strain	Pos. Breath/ participant [1]	Activity	Min (RNA/s)	25th (RNA/s)	Median (RNA/s)	75th (RNA/s)	Max (RNA/s)
Malik et al. [30]	Ancestral[1]	70/100	Breathe	1.3	4.1	Avg. 46.3	35.2	537
Ma et al. [51]	Ancestral	14/49	Breathe	28.6	—	—	—	6.3×10^3
Alsved et al. [43]	Ancestral ($n = 15$)	19/38	Breathe	0.33	—	1.15	—	3.67
	Alpha ($n = 22$)		Talk	0.5	—	1.83	—	51.67
	Unknown ($n = 1$)		Sing	0.33	—	1.33	—	130.0
Coleman et al. [44]	Ancestral ($n = 4$)	13/22	Breathe	—	0	0.04	0.126	—
	α (4), β (8),		Talk	—	0.26	0.53	1.51	—
	δ (1), κ (3), unknown (2)		Sing	—	0.15	0.79	1.35	—
Lai et al. [29]	Delta ($n = 3$)	19/32		0	—	—	—	1×10^4
	Omicron ($n = 29$)							
Zheng et al. [38]	Omicron	11/36		2.6×10^3	—	Avg. 1.4×10^4	—	5.5×10^4
Li et al. [31]	Omicron BA.5	11/27	Breathe	4.0	—	Avg. 5.6×10^3	—	3.1×10^4
Li et al. [31]	Omicron BA.2	15/51	Breathe	5.83	—	Avg. 14	—	806

[1]The strain is not explicitly stated in the paper, but samples were taken from July 18 to November 16, 2020, when the ancestral strain was dominant.

et al. [29] were able to culture 4 aerosol samples (2 delta and 2 omicron) but did not quantify them.

Santarpia et al. [46] were able to quantify RNA/PFU of 3/18 aerosol samples in the range of $0.721 \times 10^6 - 1.98 \times 10^6$ RNA/PFU. PFU and $TCID_{50}$ can be converted by a factor of 0.7 [17]. Due to the difficulties in assessing the number of infectious units in aerosol, we consider human tissue as a surrogate. Here, the contaminated mucosal fluid is more easily accessible, and infectiousness was determined in several studies. Sender et al. [32] reviewed 13 studies that measured infectious units in respiratory tract tissues of humans and monkeys and found that typical values are in the range of 10^{-5} to 10^{-3} $TCID_{50}$/RNA. Hence, we choose a ratio of 10^{-4} $TCID_{50}$/RNA for the reference case.

However, this ratio is not necessarily equal in aerosol and the respiratory tract. Schaffer et al. [54] reported that more than 90% of WSN_H influenza viruses lose infectivity during the first minute—probably during the atomization process—and Löndahl & Alsved [55] stated that changing environmental conditions (e.g., RH and temperature during exhalation) may lead to an abrupt inactivation of SARS-CoV-2. Furthermore, Hakki et al. [56] observed that the fraction was reduced by a factor of 100 during the course of infection, probably due to the increasing amount of antibodies neutralizing the virus copies. Recently, Alsved et al. [57] published the first direct measurements of the exhaled infectious virus copies in $TCID_{50}$ per second in the breath of 3 of 16 individuals. While the infectivity was below the detection limit for breathing, values from 3 to 136 $TCID_{50}$/s were emitted during talking and singing. When such data becomes available for breathing, it can be used in the model to replace the product of $\dot{R}$ and f.

2.6.4. Virus Stability s. The virus stability depends on humidity, temperature, UV radiation, and potentially other factors. Several studies have investigated the lifetime of SARS-CoV-2 in aerosol. Van Doremalen et al. [58] found an average half-life of approximately one hour. On the other hand, Fears et al. [59] observed no significant decay even after 16 h. Niazi et al. studied the effect of RH on inactivation of human rhinovirus [60] and influenza A virus [61]. They found that the salt in an aerosol particle can be crystalline or soluble in the water and that there is an RH hysteresis zone, in which the state of the salt (solid or liquid) depends on its previous state. They observed that the virus loss rate at the same RH is lower, when the aerosol comes from a low RH (when the salt is crystalline). Therefore, not only the current RH but also the previous RH can affect the loss rate. In addition, Dabisch et al. [33] performed a thorough investigation of the loss rate of SARS-CoV-2 for different combinations of temperature and relative humidity (RH). Following their research, we choose an inactivation rate of 0.6%/min, corresponding to 20°C and 20% RH, which is closest to the conditions in the Do728 aircraft cabin and not in the hysteresis zone observed by Niazi et al. [60, 61], so we expect no ambiguity in the loss rate. With the inactivation rate $\dot{d} = 0.6\%/\text{min}$, we calculate the mean stability s for all BZs in accordance with equation (4).

2.6.5. Particle Concentration in Breathing Zones C_B. The particle concentration C_B is the number of particles in the BZ divided by the volume of the BZ. We define the BZ in a hemispherical shape with a radius of 20 cm. The base of the hemisphere is tilted so that the volumes of the hemisphere and the manikin do not intersect. The center of the base is where a person's nose would be. Figure 2 illustrates four seated manikins with particles in the BZ highlighted in red, whereas the other particles are blue.

2.6.6. Inhalation Rate p_{in}. The Inhalation rate depends on age, sex, and fitness but mainly on physical activity and is lowest at total rest [41]. Since aircraft passengers are usually at rest, we assume 6 l/min for all passengers, which is a commonly chosen value for passengers in similar models/calculations [14, 62].

2.6.7. Exposure Time t_x. We choose a short-haul flight duration of 2 hours, which is typical for single-aisle passenger aircraft. Hence, the exposure time is 2 hours.

2.6.8. Dose-Response Model Based on a SARS-CoV-2 Human Challenge Study. Killingley et al. [24] conducted a human challenge study, where 34 participants were inoculated with a dose of 10 $TCID_{50}$ ancestral SARS-CoV-2, which led to the infection of 18/34 participants.

With $I(10\,\mathrm{TCID}_{50}) = 18/34$, $k_h = 7.54 \times 10^{-2}$ in equation (11), which gives the dose-response relationship:

$$I(D_{\mathrm{in}}) = V\left(1 - \exp\left(-7.54 \times {}^{-2}D_{\mathrm{in}}\right)\right). \tag{12}$$

Equation (12) is based on the assumption that each pathogen has the same probability of infecting the individual. In addition, we assume that the participants of the human challenge study are representative of the human population, which is a strong assumption given that the participants were young, healthy, and unvaccinated. However, observations by Holt et al. [63] suggest that although age is a risk factor for developing severe COVID-19, it is not a risk factor for getting infected. Under these assumptions, a dose of one $TCID_{50}$ results in a risk of infection of 7.3% in accordance with equation (12).

In the human challenge study, the inoculation dose was administered by means of nasal drops, which cover a large area of the nasal cavity and are slowly cleared to the stomach and therefore do not reach other parts of the respiratory tract [64]. The dose-response may depend on the susceptibility of the tissue of the deposition site. However, the entire human respiratory tract contains cells that express receptors required for infection with SARS-CoV-2 making the whole respiratory tract potentially susceptible [32, 65]. A similar argument was made by Henriques et al. [35] in their assessment of the risk of infection.

Lastly, the human challenge study was conducted with 10 $TCID_{50}$ of the ancestral strain. However, due to the lack of data for other strains, we use the dose-response for the ancestral strain.

2.6.9. Vulnerability of Susceptible Individuals V. The vulnerability V of individuals can be safely reduced with vaccines.

Figure 2: BZs are illustrated by black dotted lines, particles in BZ are marked in red, and the rest of the particles are indicated in blue.

The rate of protection against infection depends on the type of vaccine [66], the number of injections [67], the variant of SARS-CoV-2 (the omicron variant has particularly high immune escape capabilities [68]), the subvariant [69], and the time since the last vaccination shot [67].

Thus, assessing a realistic protection rate for the passengers on the Do728 is complex and beyond the scope of our study. Therefore, we assume a vulnerability V (unity minus protection rate) of one. This corresponds, for example, to the initial stage of the pandemic, when no one is vaccinated/recovered, or to a stage where immunity from previous infections and vaccines has completely waned.

3. Demonstration of the Infection Risk Model in an Aircraft Cabin

In the following, we estimate the risk of SARS-CoV-2 infection in a Do728 aircraft cabin to demonstrate the model. To the best of our knowledge, this is the first attempt to couple CFD particle transport with data from a human challenge study to predict the risk of SARS-CoV-2 infection.

Figure 3 shows the Do728 aircraft cabin with a single aisle, 14 rows, and five seats in each row, amounting to a total capacity of 70 passenger seats. The mixed ventilation concept is shown in Figure 4, with fresh, cool air being supplied from the ceiling and warm air exhausted near the floor for optimal passenger comfort. The relative humidity of the air during the flight is approximately 15%.

3.1. CFD Setup of the Do728 Aircraft Cabin. The flowchart in Figure 5 shows the tool chain for the CFD setup. A combination of RANS and URANS simulations, using the k-ω SST model [70] implemented in OpenFOAM, is performed to predict the flow field. Second-order upwind discretization schemes are used for the convective terms of the transport equations, and second-order central schemes are used for the other terms. The URANS is used for the initial generation of the particle cloud. After four seconds, the volatile moisture carried by the particles is completely evaporated and the momentum of the particles introduced at the beginning is dissipated. Therefore, the characteristics of the particle cloud can be copied to create new particle clouds in front of any passenger. In our study, the cloud contains 8×10^5 particles with $D(\mu\mathrm{m}) \in [0.5,50]$. The particle transport is then predicted using an OpenFOAM solver and the velocity and kinetic turbulent energy data from the RANS simulation. A similar CFD prediction using the same finite volume

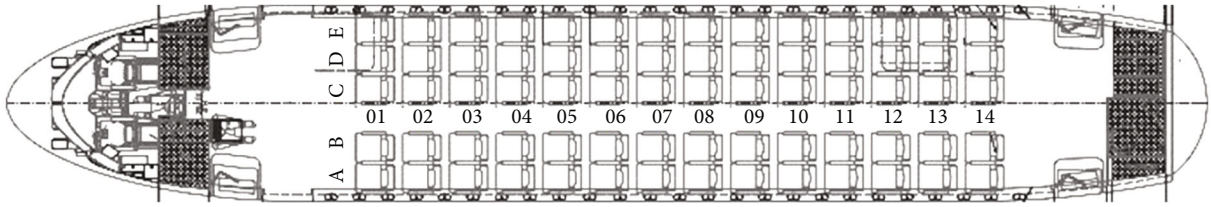

Figure 3: Sketch of the Do728 cabin layout.

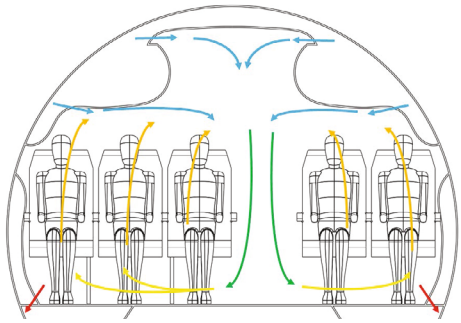

Figure 4: Mixed ventilation concept in the Do728 cabin.

method of the particle transport in a generic train compartment compared favorably with measurements in [71].

The mesh contains approximately 150 million cells with cell widths ranging from 0.5 mm in the wall layer to 20 mm in the center regions. All seats are occupied by virtual manikins, releasing 73 W of heat, thus mimicking the heat release of the human body. More information about the CFD setup can be found in [34].

3.2. Predicted Particle Transport. Figure 6 shows the particles scattered in the cabin (at the height of the BZs) after 10 minutes when the number of floating particles has reached a steady state (see Section 3.2.1). The particles in the BZs are highlighted in red, whereas the other particles are shown in blue. The figure also indicates the number of particles in each BZ. Excluding the index person (IP), most particles are found in the BZ of seat 8E, followed by seat 8D next to the source. It can be further observed that the particle concentration decreases with increasing distance from the IP and that the concentration is higher on the side of the aisle where the IP sits. In addition, the particles effectively disperse within the same row, rather than to the back or front, while the rows behind the IP still contain more particles than the rows in front of the IP.

In the following sections (3.2.1 and 3.2.2), the assumptions discussed in Section 2 will be applied to the reference case.

3.2.1. Development of the Steady State. The blue solid line in Figure 7 shows the number of particles with $D < 5\,\mu$m suspended in the air in the entire cabin over time. Additionally, a parameterized exponential function is plotted by the green dotted line, which seems to match the CFD results very well. After 50 s, the number of particles suspended in the air reaches 50% of the number of suspended particles in the steady state, while after 410 s (less than 7 minutes), the particle removal rate corresponds to 99.9% of the seeding rate. Therefore, the number of suspended particles in the cabin is nearly constant, and we consider this to be the steady state after 7 min. Since 7 min is only a small part of the total flight duration, we neglect the first 7 min and consider only the steady-state phase.

3.2.2. Influence of the Particle Size. Figure 8 shows the particle size distribution in all seat rows except for row 1 and row 2 due to insufficient particle counts. The horizontal cross sections of the seat rows are illustrated in Figure 6 by black dotted lines, where all particles between the floor and the ceiling are counted. The markers in Figure 8 represent the data, while the lines have no physical meaning and connect markers of the same seat row for illustration purposes. Eight different size bins are indicated by the gray dotted vertical lines.

The PSD of the source is constant in the simulation (not shown in Figure 8). Thus, if the particle size had an effect on the particle transport, the PSDs in the domain would not be expected to be constant. This is only observed for particles with $D > 5\,\mu$m, with a clear declining trend in number density with increasing diameter. This is plausible as larger particles are more likely to settle down due to a higher mass to drag ratio. In contrast, no significant differences are observed between the four bins $< 5\,\mu$m in any seat row. This shows that the number of particles per size bin is nearly constant in each seat row. The blue markers connected by the blue line illustrate the geometric mean, which is also nearly constant for $D < 5\,\mu$m but shows a decreasing trend for $D > 5\,\mu$m.

In summary, for $D < 5\,\mu$m, the particle size distributions in the seat rows are constant, i.e., proportional to the PSD of the source. This confirms the finding of Bivolarova et al. [42] that particles of any size $< 5\,\mu$m are equally likely to be transported to any seat row and, therefore, that viruses carried by, e.g., 1 μm particles end up in the same locations as viruses carried by, e.g., 4 μm particles. Consequently, the particle diameter has no significant influence on the virus transport in the considered scenario (geometry, boundary conditions). Although particles $> 5\,\mu$m behave differently than the smaller ones, these larger particles are less relevant for the transport of virions as they carry only a minor fraction of RNA copies (see Section 2.6).

3.3. Virus Stability in the Breathing Zones. Figure 9 shows the mean stability in each BZ—containing at least one particle—resulting from the assumed loss rate of 0.6%/min. The trend shown is similar to particle dispersion: the further away from the IP, the lower the virus stability (due to longer travel time). More than 99% of the virions remain active

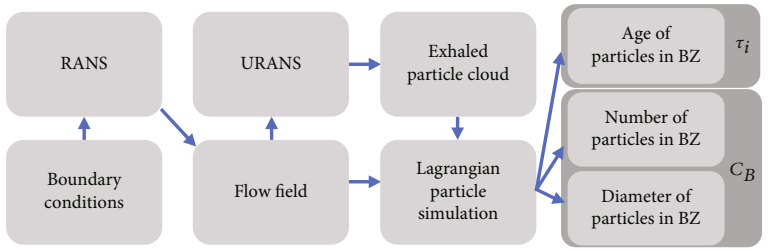

Figure 5: Flowchart of the numerical simulations: first, the boundary conditions are defined and the flow field is predicted by a RANS simulation. This flow field is used as the initial condition for a URANS simulation, where particles are exhaled and partially evaporated and their momentum dissipated to form a particle cloud. The characteristics of the resulting particle cloud are then used as the initial condition for the Lagrangian particle transport simulation in the RANS flow field.

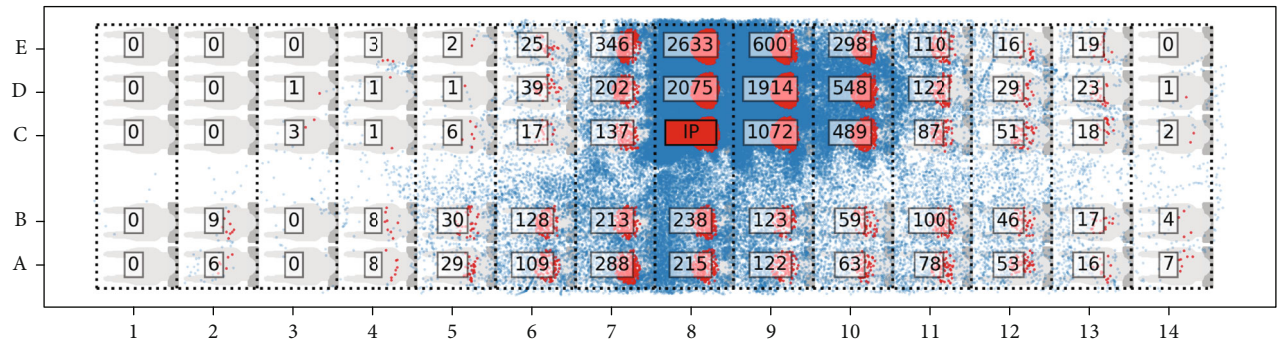

Figure 6: Scatterplot of particles at the height of 1 m to 1.5 m. The particles in the BZs are highlighted in red, and the number of particles in the BZ is indicated on the corresponding BZ.

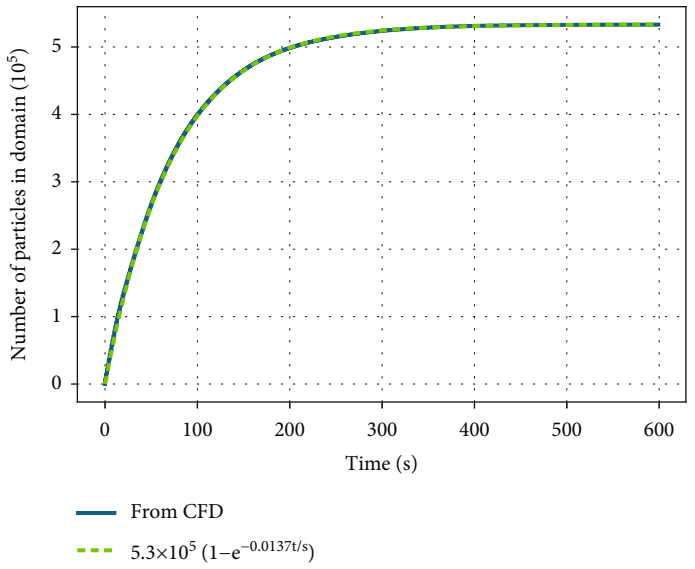

Figure 7: Development of the number of particles in the cabin over time compared to a parameterized function.

near the IP (e.g., seats 8D, 8E, and 9C). The lowest value is found at seat 14A, where 96.0% of the infectious virions remain active during transport. This reveals that the biological decay of SARS-CoV-2 is insignificant in the Do728 aircraft cabin. The low relative humidity and temperature favor virus stability. In addition, the high air change rate removes virus-laden particles before a significant amount of virions is inactivated.

3.4. Inhaled Dose and Infection Risk. Figure 10 shows the inhaled infectious dose for each passenger, calculated using the dose inhalation rate obtained from equation (5) and the assumed exposure time of 2 hours. As expected, the doses follow the same trend as the particle dispersion—with the highest values found near the IP and the lowest values in the two front rows. The values shown here should be considered as expected or mean values, since the number of

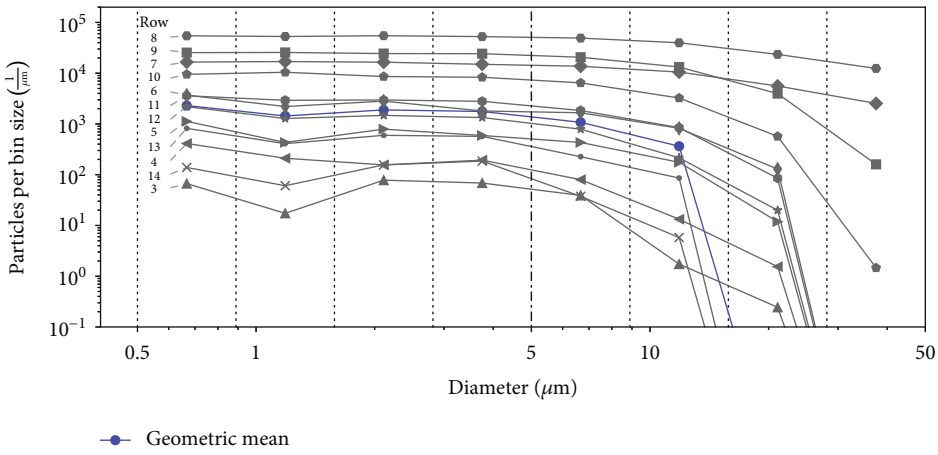

Figure 8: PSDs in seat rows (row 1 and 2 excluded due to low number of particles). Values of zero ($10^{-\infty}$)/μm are set to 10^{-4}/μm for better illustration (does not affect any shown marker, but lines crossing the horizontal axis would otherwise be vertical and overlapping).

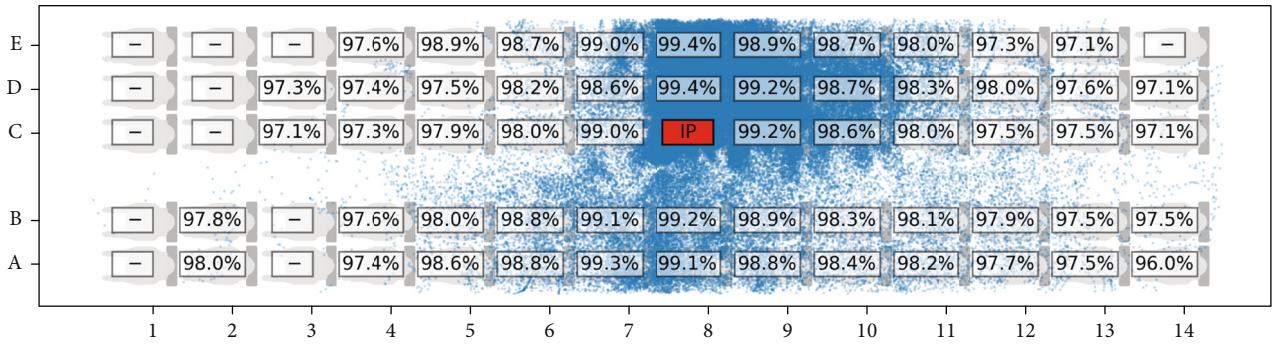

Figure 9: Mean biological stability in BZs.

infectious virions is discrete (e.g., 0 or 1) and cannot attain decimal values such as 0.78, as found at seat 8E. This could also be interpreted as a 78% probability to inhale a dose of 1 $TCID_{50}$. Of note, 0.78 is the highest infectious dose observed. This means that no passenger is expected to inhale an infectious dose of 2 $TCID_{50}$ or more.

Figure 11 shows the risk of infection derived from the infectious dose calculated with equation (10) for all seats. The highest risk of infection is observed at seat 8E with a probability of 5.72% followed by seat 8D with 4.53%. The risk of infection for the passengers in the row in front of the IP is lower than 1%, whereas in the row behind the IP, the risk of infection is up to 4.18% on seat 9D. The aisle seems to have a protective effect, as the maximum risk on the A and B seats is 0.64% on seat 7A. While the risk of infection on the A and B seats is lowest for the rows near the IP, the opposite is true for the rows further away from the IP. For example, in rows 5, 6, and 12, the risk of infection is highest on the A and B seats.

3.5. Sensitivity Analysis. The risk of infection shown in Figure 11 depends on several parameters that cannot be clearly defined but may vary from case to case and from person to person. Table 2 provides an overview of the possible ranges for the different parameters. Most importantly, the virus emission rate of an infected individual could vary from 0 to 5.5×10^4 RNA copies emitted each second. The fraction of $TCID_{50}$ per RNA copy also varies over three orders of magnitude between 10^{-6} and 10^{-3}. Since, in accordance with equation (5), the inhaled infectious dose is directly proportional to these two parameters, the inhaled infectious dose could vary by several orders of magnitude, depending on the selected values for each parameter. Thus, we perform a sensitivity analysis to examine the situation in the Do728 aircraft cabin for the reference case and other selected values. Figure 12 shows the probability of 0, 1, and >2 secondary infections for the reference case discussed above (reference dose factor = 1).

In the reference case, the probability of two or more transmissions is 3.07%, the probability of 1 transmission is 21.85%, and the probability of no transmission is 75.08%. Reminder: only inhaled doses of zero or one $TCID_{50}$ are expected in the reference case. This means that the individuals infected in this scenario inhaled only a single $TCID_{50}$.

We chose a virus emission rate of 5×10^2 RNA/s. However, if the virus emission rate was 100 times higher, as observed by Zheng et al. [38], for example, the inhaled infectious dose would also be 100 times higher. Therefore, the "reference dose factor" (RDF) would be 100, and the model would predict at least two transmissions. The blue dotted

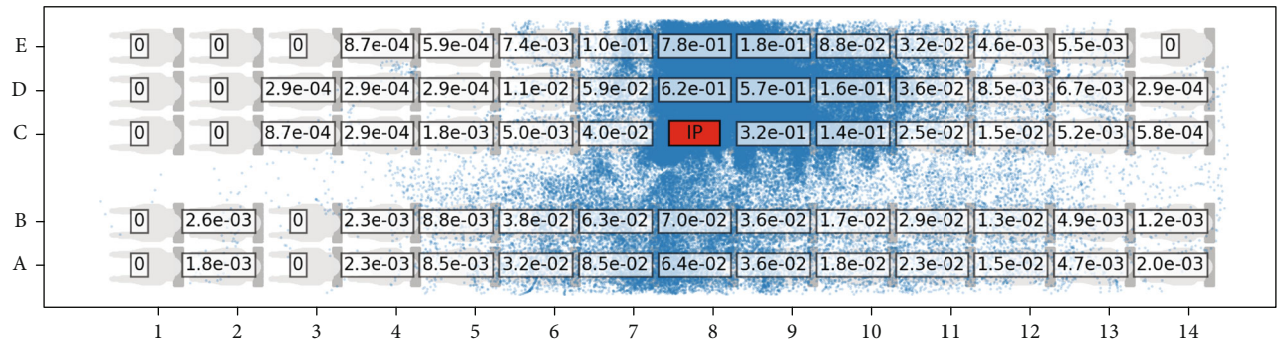

Figure 10: Infectious dose $\dot{D}_{in}$ ($TCID_{50}$) inhaled during the duration of the flight.

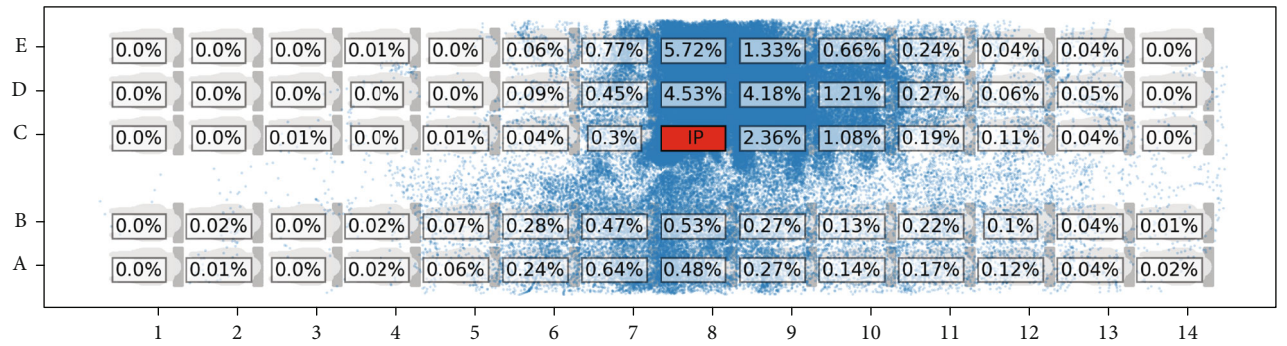

Figure 11: Infection risk of individual passengers.

Table 2: Summary of selected values for the reference case.

Parameter	Symbol	Possible range	Reference case
Virus emission	$\dot{R}$	$0 - 5.5 \times 10^4$ RNA/s	500 RNA/s
$TCID_{50}$/RNA	f	$10^{-6} - 10^{-3}$	10^{-4}
Inactivation rate	$\dot{d}$	0.0-6.4%/min	0.6%/min
Flight duration	t_x	0.5-18.5 h	2 h
Inhalation rate	p_{in}	6-54 l/min	6 l/min
Vulnerability	V	0-1	1

line in Figure 12 also shows the number of expected infections on the right-hand y-axis. For the reference case (RDF = 1), the model predicts less than one infection. In contrast, for a 100 times higher dose (RDF = 100), 12 infections are predicted. On the other hand, the highest virus emission for breathing observed by Alsved et al. [43] is only 3.67 RNA/s. With this value, the RDF would be less than 10^{-2} resulting in a risk of infection close to zero. This shows the importance of choosing the right values and highlights the importance of the person-to-person variation in virus emission. Knowing that a person sitting in seat 8C is SARS-CoV-2 positive could result in 0 to 12 infections, depending on their virus emission rate. Even more than 12 infections are possible with an RDF > 100, e.g., with a 100-fold virus emission and a 10-fold f. Thus, a probability density function of the virus emission rate would be helpful, to model the probability of the IP being a low, medium, or high emitter. Sawano et al. [50] found such a PDF to have a log-normal shape—however, with a very limited number of participants. Henriques et al. [35] used the distribution of the viral load in the upper respiratory tract, for which there is ample data [49], and 10% of cases have a 100-fold higher viral load compared to the median. However, as we pointed out above, the viral load in the upper respiratory tract does not necessarily correlate with the number of exhaled virions.

Based on the RDF, any other combination of values can be quickly evaluated; e.g., a 5 times longer flight time (10 h) and 10% of the virus emission of the reference case (50 RNA/s) would result in an RDF of 0.5 and approximately a 13% chance of one transmission.

3.5.1. Loss Rate and Mean Stability. While the mean stability is proportional to the inhaled infectious dose and can therefore be easily evaluated with the RDF, the loss rate is not proportional to the mean stability (see equation (4)). The loss rate can be looked up in the literature, but how it translates into the mean stability depends on the individual travel time of the particles. Figure 13 shows the relationship between the loss rate and the virus stability for the Do728 cabin. The figure shows the relationship for the BZs—with at least one CFD particle—in light gray lines. It take particles the longest to reach seat 14A. Therefore, the loss rate has the greatest impact on this seat: at a loss rate of 20%/min, only approximately 22% of the particles remain active after being transported to the BZ. In contrast, the particles in the BZ of

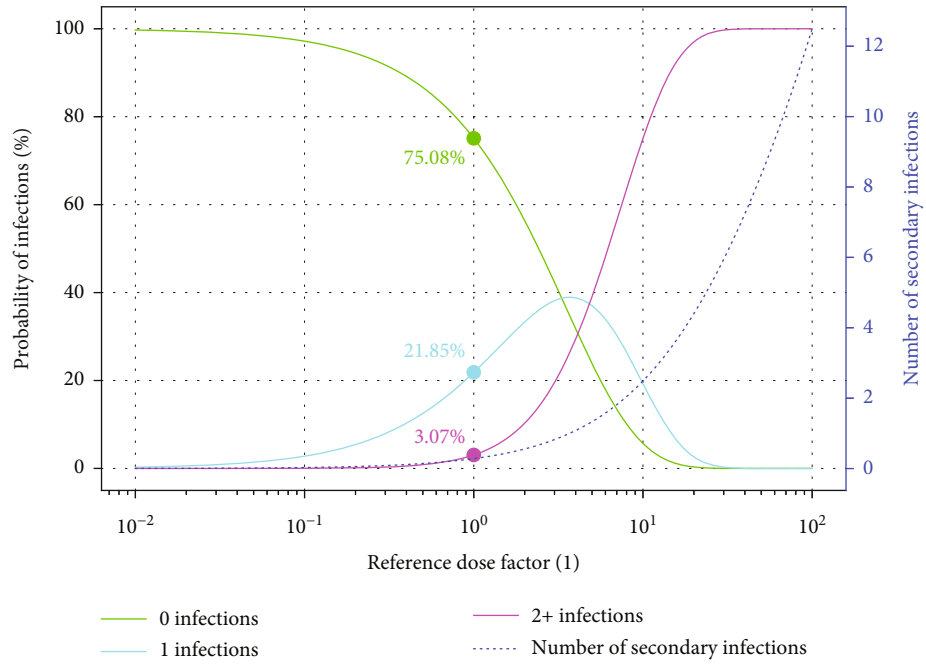

Figure 12: Estimated number of secondary infections for doses of 10^{-2} to 10^{2} times the dose of the reference case.

seat 8E have the shortest travel time, and at a 20%/min loss rate, 80% of the particles still remain active. The figure also shows the median and average stability; both are approximately 50% at a loss rate of 20%/min. Dabisch et al. [33] found that the loss rate of SARS-CoV-2 increases with higher temperature and higher relative humidity. For 70% relative humidity (RH) at 30°C, they observed a loss rate of 6.4%. These conditions are not typical of aircraft cabins, but at this loss rate, the average and median survival rate are approximately 90%. Therefore, they would reduce the RDF by a factor of about 0.9 (compared to no decay) and have a small but noticeable impact on the risk of infection. Nevertheless, compared to the possible range of other parameters, such as flight time, virus emission rate, and fraction of $TCID_{50}$/RNA, the impact of the biological decay on SARS-CoV-2 transmission in the Do728 cabin is insignificant.

4. Discussion

In contrast to the usual backward quantum calculation from known outbreaks, the proposed model predicts the risk of infection by means of a "forward" calculation. This requires several parameters from the literature. For example, if virus-laden particles of different sizes are transported to different regions, e.g., because the larger particles settle faster, then the concentration of virus copies per ml for different size bins would be required. This data is currently scarce, but a simplification can be made by assuming that the particle size does not affect the particle transport, thus rendering the virus concentration unnecessary. We have shown that this assumption holds true for SARS-CoV-2 virions emitted by breathing in the Do728 aircraft cabin, since particles smaller than 5 μm behave in a sufficient similar way and particles larger than 5 μm carry only a minor fraction of the viable virions. The simplified model still requires virus-specific data from the literature: virus emission rate, fraction of $TCID_{50}$ per RNA, biological loss rate, and dose-response. In the typical Wells-Riley model, all these parameters are combined in the quanta, since one quantum is defined as the number of particles representing a risk of infection of ≈63%. The quantum emission rate is typically calculated backward from known events, using the well-mixed room assumption. While this allows all the necessary data to be gathered from a single event, important information about virus-laden particle size, particle dispersion, and the virus-specific parameters is lost. This is particularly problematic when considering the high person-to-person variation in virus emission. In the backward calculation, it is not possible to determine whether many people were infected due to unfavorable airflow (or seat positions), high virus emission rate, high fraction of $TCID_{50}$/RNA, high virus stability, high dose-response, or pure chance.

In contrast, the presented approach offers the possibility to vary the virus-specific parameters individually. This allows to consider different virus emission rates of weak and strong emitters and to study superspreaders. We used the virus emission rate measured directly in the exhaled aerosol, instead of calculating it from the virus concentration in the upper respiratory tract. Moreover, the reference dose factor allows a quick sensitivity analysis of the individual parameters. Finally, the airflow and particle transport are predicted by CFD simulations instead of assuming a well-mixed room. The main drawback of this approach is the extensive data gathering and the uncertainty of the virus-specific parameters, which may also raise ethical questions, especially for the dose-response based on human challenge data.

While many studies focus on unsteady respiratory events—such as coughing or sneezing—we investigate virus

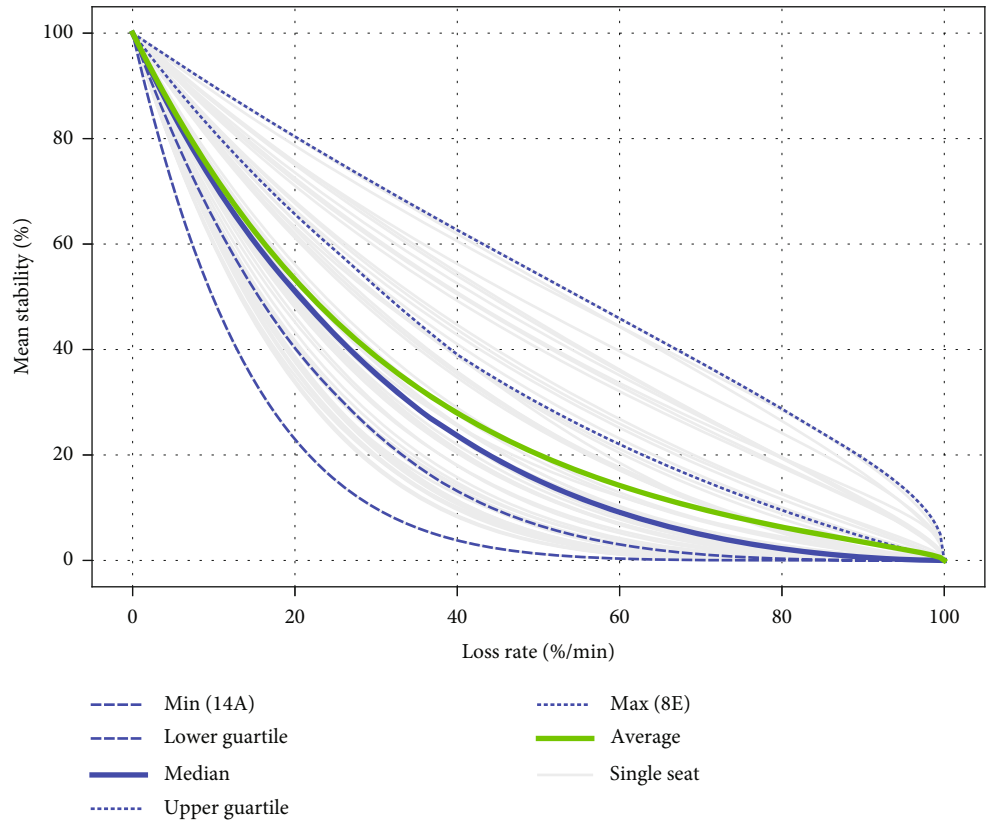

Figure 13: Mean virus stability in the BZs over biological loss rate in the Do728 aircraft cabin.

emission during normal breathing since SARS-CoV-2 is often transmitted by pre- and asymptomatic individuals. Coughing or sneezing can release many RNA copies at once, whereas the continuous emission during breathing leads to an accumulation of respiratory particles in the air over time. Our CFD results show that in an aircraft cabin with typical ventilation, a steady state is reached after about 7 min and 50% of the final particle concentration is reached after 50 s.

The particle dispersion in the Do728 aircraft cabin shows that the particle concentration reaches the highest values near the IP, especially on the same side of the aisle as the IP. The same trend is observed for virus stability, inhaled infectious dose, and consequently risk of infection. This shows that the risk of airborne transmission becomes negligible with increasing distance even though aerosol particles are capable of occasionally traveling long distances and remaining airborne for long periods of time. This implies that maintaining distance is helpful not only in case of larger ballistic droplets but also against airborne particles, at least for the considered scenario. In the case of SARS-CoV-2, the virus emissions rates in the literature range from 0 to 5.5×10^4 RNA/s, resulting in a wide possible range of 0-12 expected infections. In addition, the fraction of $TCID_{50}$ per RNA can vary by a factor of 100 during the course of infection. After the biological inactivation during transport into the breathing zones, at least 96% of the virions remain active, showing that biological decay is not significant in the considered case. However, the model is capable of modeling the biological inactivation. And at lower air change rates—hence longer residence times and different climatic conditions—the biological inactivation could become significant. Furthermore, other viruses or bacteria may have higher loss rates, which could make biological inactivation more relevant.

Due to the large possible range of predicted infection risks, caused by the uncertainty in the input parameters, validation of the model is difficult. To properly validate the model, known outbreaks are not sufficient, as we would also need to know, for example, the virus emission rate and fraction of $TCID_{50}$ per RNA of the index person during that outbreak. We are not aware of the existence of such data. However, without knowing the virus emission rate, we could assume any virus emission rate in the range from 0 to 5.5×10^4 RNA/s to obtain the desired risk of infection, which would be a validation of the parameter values rather than the model itself. In summary, the high person-to-person variability and the ethical problems of controlled experiments with humans make validation unfeasible. However, the same problem arises for the backward quantum calculation.

Finally, since the model treats virus-specific parameters individually, the risk of infection with a hypothetical mutation with a different value in a single virus-specific parameter can be estimated.

4.1. Limitations. Several assumptions and approximations lead to the presented results. We expect the largest discrepancies between the model prediction and the actual risk to

be due to the following: uncertainties in the virus-specific parameters discussed above possibly lead to the largest uncertainties in the predicted risk of infection. In addition, due to the lack of data, we mixed virus-specific parameters from different SARS-CoV-2 strains, e.g., the dose-response from the ancestral strain with virus emission from later variants. In addition, we assume that the (unvaccinated) participants in the human challenge are representative of the whole population. Lastly, we assume a steady flow field in the aircraft cabin for the particle transport to reduce computational resources and perform a RANS simulation.

5. Conclusion

We present a model that directly estimates the risk of infection, as opposed to the backward quantification required in the Wells-Riley model. The model captures relevant pathogen-specific parameters, such as the biological loss rate and the pathogen emission rate, as well as pathogen-independent parameters, such as the particle transport, the inhalation rate, and the exposure time. Since the particle size has no significant effect on particle transport for the considered particles ($<5\,\mu$m), the available data is sufficient to apply the model for SARS-CoV-2.

To the best of our knowledge, this is the first coupling of dose-response data from a SARS-CoV-2 human challenge study and particle transport predicted by CFD to predict the risk of infection. We have applied the model to predict the risk of SARS-CoV-2 infections in a Do728 aircraft cabin and draw the following conclusions:

(i) SARS-CoV-2 human challenge data can be used to estimate the risk of infection in aircraft cabins by "forward" calculation

(ii) The model captures the local risk of infection: the highest risk was observed in the same row, on the same side of the aisle as the index person. The risk of infection decreases rapidly with increasing distance from the index person

(iii) The model captures biological decay: at least 96% of active virions remain active during particle transport. While this is less significant in this particular scenario, biological inactivation could be relevant in other circumstances, such as different ventilation rates or different pathogens

(iv) Particle size only has a minor impact on SARS-CoV-2-laden aerosol transport in the Do728 cabin, thus allowing for a simplification of the model

(v) The high person-to-person variability, e.g., in the virus emission rate, results in a wide range of possible outcomes from 0 to at least 12 subsequent infections. This poses a challenge in selecting the values for the model's input parameters but provides the opportunity to better investigate the effect of superspreaders more efficiently

(vi) The sensitivity analysis offers the possibility to perform a quick assessment of the potential risk of infection in the aircraft cabin if different values were chosen for the input parameters

The accuracy of the model is highly dependent on the values of the input parameters. Therefore, only if the required data is available does the proposed model represent an alternative to the common Wells-Riley model with reverse quantum calculation. In this case, the individual influences of the virus-specific parameters can be modeled with the presented method, which is not possible with the quantum method. This also highlights the importance of fast data collection with regard to virus emission rate, fraction of infectious units in the exhaled breath, loss rate in aerosol, and dose-response when a new airborne disease emerges.

Data Availability

Data are available on request.

Conflicts of Interest

The authors declare no conflicts of interest.

Acknowledgments

This work was funded by the GANDALF project (2475064) of the German Aerospace Center (DLR). Open Access funding enabled and organized by Projekt DEAL.

References

[1] R. Zhang, Y. Li, A. L. Zhang, Y. Wang, and M. J. Molina, "Identifying airborne transmission as the dominant route for the spread of COVID-19," *Proceedings of the National Academy of Sciences*, vol. 117, no. 26, pp. 14857–14863, 2020.

[2] H. Nishiura, H. Oshitani, T. Kobayashi et al., *Closed Environments Facilitate Secondary Transmission of Coronavirus Disease 2019 (COVID-19)*, medRxiv, 2020.

[3] W. F. Wells, *Airborne Contagion and Air Hygiene: An Ecological Study of Droplet Infections*, Commonwealth Fund, 1955.

[4] E. C. Riley, G. Murphy, and R. L. Riley, "Airborne spread of measles in a suburban elementary school," *American Journal of Epidemiology*, vol. 107, no. 5, pp. 421–432, 1978.

[5] Z. Wang, E. R. Galea, A. Grandison, J. Ewer, and F. Jia, "A coupled computational fluid dynamics and Wells-Riley model to predict COVID-19 infection probability for passengers on long-distance trains," *Safety Science*, vol. 147, article 105572, 2022.

[6] Y. Shang, J. Dong, L. Tian, F. He, and J. Tu, "An improved numerical model for epidemic transmission and infection risks assessment in indoor environment," *Journal of Aerosol Science*, vol. 162, article 105943, 2022.

[7] J. K. Gupta, C.-H. Lin, and Q. Chen, "Risk assessment of airborne infectious diseases in aircraft cabins," *Indoor Air*, vol. 22, no. 5, pp. 388–395, 2012.

[8] C. Sun and Z. Zhai, "The efficacy of social distance and ventilation effectiveness in preventing COVID-19 transmission," *Sustainable Cities and Society*, vol. 62, article 102390, 2020.

[9] G. Buonanno, L. Stabile, and L. Morawska, "Estimation of airborne viral emission: quanta emission rate of sars-cov-2 for infection risk assessment," *Environment International*, vol. 141, article 105794, 2020.

[10] Z. Zhang, T. Han, K. H. Yoo, J. Capecelatro, A. L. Boehman, and K. Maki, "Disease transmission through expiratory aerosols on an urban bus," *Physics of Fluids*, vol. 33, no. 1, article 015116, 2021.

[11] M. Konstantinov and C. Wagner, "Numerical simulation of the thermal comfort in a train cabin," *International Journal of Railway Technology*, vol. 4, no. 3, pp. 69–88, 2015.

[12] D. Schmeling, M. Kühn, D. Schiepel et al., "Analysis of aerosol spreading in a German inter city express (ICE) train carriage," *Building and Environment*, vol. 222, article 109363, 2022.

[13] N. Shinohara, J. Sakaguchi, H. Kim et al., "Survey of air exchange rates and evaluation of airborne infection risk of COVID-19 on commuter trains," *Environment International*, vol. 157, article 106774, 2021.

[14] H. Woodward, S. Fan, R. K. Bhagat et al., "Air flow experiments on a train carriage—towards understanding the risk of airborne transmission," *Atmosphere*, vol. 12, no. 10, p. 1267, 2021.

[15] J. K. Gupta, C.-H. Lin, and Q. Chen, "Transport of expiratory droplets in an aircraft cabin," *Indoor Air*, vol. 21, no. 1, pp. 3–11, 2011.

[16] R. You, C.-H. Lin, D. Wei, and Q. Chen, "Evaluating the commercial airliner cabin environment with different air distribution systems," *Indoor Air*, vol. 29, no. 5, pp. 840–853, 2019.

[17] A. Mikszewski, L. Stabile, G. Buonanno, and L. Morawska, "The airborne contagiousness of respiratory viruses: a comparative analysis and implications for mitigation," *Geoscience Frontiers*, vol. 13, no. 6, article 101285, 2022.

[18] H. Dai and B. Zhao, "Association of the infection probability of COVID-19 with ventilation rates in confined spaces," *Building Simulation*, vol. 13, no. 6, pp. 1321–1327, 2020.

[19] M. Hu, H. Lin, J. Wang et al., "Risk of coronavirus disease 2019 transmission in train passengers: an epidemiological and modeling study," *Clinical Infectious Diseases*, vol. 72, no. 4, pp. 604–610, 2021.

[20] F. Pourfattah, L.-P. Wang, W. Deng, Y.-F. Ma, L. Hu, and B. Yang, "Challenges in simulating and modeling the airborne virus transmission: a state-of-the-art review," *Physics of Fluids*, vol. 33, no. 10, article 101302, 2021.

[21] N. B. McCullough and C. W. Eisele, "Experimental human salmonellosis: I. Pathogenicity of strains of Salmonella meleagridis and Salmonella anatum obtained from spray-dried whole egg," *Journal of Infectious Diseases*, vol. 88, no. 3, pp. 278–289, 1951.

[22] H. L. DuPont, R. B. Hornick, A. T. Dawkins, M. J. Snyder, and S. B. Formal, "The response of man to virulent Shigella flexneri 2a," *The Journal of Infectious Diseases*, vol. 119, no. 3, pp. 296–299, 1969.

[23] R. L. Ward, D. I. Bernstein, E. C. Young, J. R. Sherwood, D. R. Knowlton, and G. M. Schiff, "Human rotavirus studies in volunteers: determination of infectious dose and serological response to infection," *Journal of Infectious Diseases*, vol. 154, no. 5, pp. 871–880, 1986.

[24] B. Killingley, A. J. Mann, M. Kalinova et al., "Safety, tolerability and viral kinetics during SARS-CoV-2 human challenge in young adults," *Nature Medicine*, vol. 28, no. 5, pp. 1031–1041, 2022.

[25] M. L. Pöhlker, O. O. Krüger, J.-D. Förster et al., "Respiratory Aerosols and Droplets in the Transmission of Infectious Diseases," *Reviews of Modern Physics*, Aemerican Physical Society (APS), 2021.

[26] M. Alsved, D. Nygren, S. Thuresson, C. J. Fraenkel, P. Medstrand, and J. Löndahl, "Size distribution of exhaled aerosol particles containing SARS-CoV-2 RNA," *Infectious Diseases*, vol. 55, no. 2, pp. 158–163, 2023.

[27] G. Bagheri, B. Thiede, B. Hejazi, O. Schlenczek, and E. Bodenschatz, "An upper bound on one-to-one exposure to infectious human respiratory particles," *Proceedings of the National Academy of Sciences*, vol. 118, no. 49, article e2110117118, 2021.

[28] Y. Yan, X. Li, X. Fang, Y. Tao, and J. Tu, "A spatiotemporal assessment of occupants' infection risks in a multi-occupants space using modified Wells-Riley model," *Building and Environment*, vol. 230, article 110007, 2023.

[29] J. Lai, K. K. Coleman, S. H. S. Tai et al., "Exhaled Breath Aerosol Shedding of Highly Transmissible Versus Prior Severe Acute Respiratory Syndrome Coronavirus 2 Variants," *Clinical Infectious Diseases*, vol. 76, no. 5, pp. 786–794, 2023.

[30] M. Malik, A.-C. Kunze, T. Bahmer, S. Herget-Rosenthal, and T. Kunze, "SARS-CoV-2: viral loads of exhaled breath and oronasopharyngeal specimens in hospitalized patients with COVID-19," *International Journal of Infectious Diseases*, vol. 110, pp. 105–110, 2021.

[31] J. Li, J. Zheng, P. Chen et al., "Higher SARS-CoV-2 shedding in exhaled aerosol probably contributed to the enhanced transmissibility of omicron BA.5 subvariant," *Journal of Medical Virology*, vol. 95, no. 1, article e28365, 2023.

[32] R. Sender, Y. M. Bar-On, S. Gleizer et al., "The total number and mass of SARS-CoV-2 virions," *Proceedings of the National Academy of Sciences*, vol. 118, no. 25, 2021.

[33] P. Dabisch, M. Schuit, A. Herzog et al., "The influence of temperature, humidity, and simulated sunlight on the infectivity of SARS-CoV-2 in aerosols," *Aerosol Science and Technology*, vol. 55, no. 2, pp. 142–153, 2021.

[34] D. Schmeling, A. Shishkin, D. Schiepel, and C. Wagner, "Numerical and Experimental Study of Aerosol Dispersion in the do728 Aircraft Cabin," *CEAS Aeronautical Journal*, vol. 14, no. 2, pp. 509–526, 2023.

[35] A. Henriques, N. Mounet, L. Aleixo et al., "Modelling airborne transmission of sars-cov-2 using CARA: risk assessment for enclosed spaces," *Interface Focus*, vol. 12, no. 2, article 20210076, 2022.

[36] D. Pan, C. M. Williams, J. Decker et al., "Exhaled SARS-CoV-2 RNA viral load kinetics measured by facemask sampling associates with household transmission," *Clinical Microbiology and Infection*, vol. 29, no. 2, pp. 254.e1–254.e6, 2023.

[37] M. Nicas, W. W. Nazaroff, and A. Hubbard, "Toward understanding the risk of secondary airborne infection: emission of respirable pathogens," *Journal of Occupational and Environmental Hygiene*, vol. 2, no. 3, pp. 143–154, 2005.

[38] J. Zheng, Z. Wang, J. Li et al., "High amounts of SARS-CoV-2 in aerosols exhaled by patients with omicron variant infection," *Journal of Infection*, vol. 84, no. 6, pp. e126–e128, 2022.

[39] Y. Yan, X. Li, Y. Shang, and J. Tu, "Evaluation of airborne disease infection risks in an airliner cabin using the Lagrangian-based Wells-Riley approach," *Building and Environment*, vol. 121, pp. 79–92, 2017.

[40] S. Elghobashi, "On predicting particle-laden turbulent flows," *Applied Scientific Research*, vol. 52, no. 4, pp. 309–329, 1994.

[41] W. C. Hinds, *Aerosol Technology: Properties, Behavior, and Measurement of Airborne Particles*, John Wiley & Sons, 1999.

[42] M. Bivolarova, J. Ondráček, A. Melikov, and V. Ždímal, "A comparison between tracer gas and aerosol particles distribution indoors: the impact of ventilation rate, interaction of airflows, and presence of objects," *Indoor Air*, vol. 27, no. 6, pp. 1201–1212, 2017.

[43] M. Alsved, D. Nygren, S. Thuresson, P. Medstrand, C. J. Fraenkel, and J. Löndahl, "SARS-CoV-2 in exhaled aerosol particles from COVID-19 cases and its association to household transmission," *Clinical Infectious Diseases*, vol. 75, no. 1, pp. e50–e56, 2022.

[44] K. K. Coleman, D. J. W. Tay, K. S. Tan et al., "Viral load of severe acute respiratory syndrome coronavirus 2 (SARS-CoV-2) in respiratory aerosols emitted by patients with coronavirus disease 2019 (COVID-19) while breathing, talking, and singing," *Clinical Infectious Diseases*, vol. 74, pp. 1722–1728, 2022.

[45] J. A. Lednicky, M. Lauzardo, M. M. Alam et al., "Isolation of SARS-CoV-2 from the air in a car driven by a COVID patient with mild illness," *International Journal of Infectious Diseases*, vol. 108, pp. 212–216, 2021.

[46] J. L. Santarpia, V. L. Herrera, D. N. Rivera et al., "The size and culturability of patient-generated SARS-CoV-2 aerosol," *Journal of Exposure Science & Environmental Epidemiology*, vol. 32, no. 5, pp. 706–711, 2022.

[47] M. Kriegel, A. Hartmann, U. Buchholz, J. Seifried, S. Baumgarte, and P. Gastmeier, "SARSCoV-2 aerosol transmission indoors: a closer look at viral load, infectivity, the effectiveness of preventive measures and a simple approach for practical recommendations," *International Journal of Environmental Research and Public Health*, vol. 19, no. 1, p. 220, 2022.

[48] J. Zhou, A. Singanayagam, N. Goonawardane et al., "Viral emissions into the air and environment after SARS-CoV-2 human challenge: a phase 1, open label, first-in-human study," *The Lancet Microbe*, vol. 4, 2022.

[49] D. Jacot, G. Greub, K. Jaton, and O. Opota, "Viral load of SARS-CoV-2 across patients and compared to other respiratory viruses," *Microbes and Infection*, vol. 22, no. 10, pp. 617–621, 2020.

[50] M. Sawano, K. Takeshita, H. Ohno, and H. Oka, "SARS-CoV-2 RNA load and detection rate in exhaled breath condensate collected from COVID-19 patients infected with delta variant," *Journal of Breath Research*, vol. 16, no. 3, article 036006, 2022.

[51] J. Ma, X. Qi, H. Chen et al., "Coronavirus disease 2019 patients in earlier stages exhaled millions of severe acute respiratory syndrome coronavirus 2 per hour," *Clinical Infectious Diseases*, vol. 72, no. 10, pp. e652–e654, 2021.

[52] J. Zhou, J. A. Otter, J. R. Price et al., "Investigating severe acute respiratory syndrome coronavirus 2 (SARS-CoV-2) surface and air contamination in an acute healthcare setting during the peak of the coronavirus disease 2019 (COVID-19) pandemic in London," *Clinical Infectious Diseases*, vol. 73, no. 7, pp. e1870–e1877, 2021.

[53] O. O. Adenaiye, J. Lai, P. J. Bueno de Mesquita et al., "Infectious severe acute respiratory syndrome coronavirus 2 (SARS-CoV-2) in exhaled aerosols and efficacy of masks during early mild infection," *Clinical Infectious Diseases*, vol. 75, no. 1, pp. e241–e248, 2022.

[54] F. L. Schaffer, M. E. Soergel, and D. C. Straube, "Survival of airborne influenza virus: effects of propagating host, relative humidity, and composition of spray fluids," *Archives of Virology*, vol. 51, no. 4, pp. 263–273, 1976.

[55] J. Löndahl and M. Alsved, "Abrupt decreases in infectivity of SARS-CoV-2 in aerosols," *Proceedings of the National Academy of Sciences*, vol. 119, no. 29, article e2208742119, 2022.

[56] S. Hakki, J. Zhou, J. Jonnerby et al., "Onset and window of SARS-CoV-2 infectiousness and temporal correlation with symptom onset: a prospective, longitudinal, community cohort study," *The Lancet Respiratory Medicine*, vol. 10, no. 11, pp. 1061–1073, 2022.

[57] M. Alsved, K. Nyström, S. Thuresson et al., "Infectivity of exhaled sars-cov-2 aerosols is sufficient to transmit COVID-19 within minutes," *Scientific Reports*, vol. 13, no. 1, p. 21245, 2023.

[58] N. van Doremalen, T. Bushmaker, D. H. Morris et al., "Aerosol and surface stability of SARS-CoV-2 as compared with SARS-CoV-1," *New England Journal of Medicine*, vol. 382, no. 16, pp. 1564–1567, 2020.

[59] A. C. Fears, W. B. Klimstra, P. Duprex et al., "Persistence of severe acute respiratory syndrome coronavirus 2 in aerosol suspensions," *Emerging Infectious Diseases*, vol. 26, no. 9, pp. 2168–2171, 2020.

[60] S. Niazi, R. Groth, L. Cravigan et al., "Susceptibility of an airborne common cold virus to relative humidity," *Environmental Science & Technology*, vol. 55, no. 1, pp. 499–508, 2021.

[61] S. Niazi, K. R. Short, R. Groth et al., "Humidity-dependent survival of an airborne influenza a virus: practical implications for controlling airborne viruses," *Environmental Science & Technology Letters*, vol. 8, no. 5, pp. 412–418, 2021.

[62] J. Pantelic, G. N. Sze-To, K. W. Tham, C. Y. H. Chao, and Y. C. M. Khoo, "Personalized ventilation as a control measure for airborne transmissible disease spread," *Journal of The Royal Society Interface*, vol. 6, Supplement_6, pp. S715–S726, 2009.

[63] H. Holt, M. Talaei, M. Greenig et al., "Risk factors for developing COVID-19: a population-based longitudinal study (COVIDENCE UK)," *Thorax*, vol. 77, no. 9, pp. 900–912, 2022.

[64] J. G. Hardy, S. W. Lee, and C. G. Wilson, "Intranasal drug delivery by spray and drops," *Journal of Pharmacy and Pharmacology*, vol. 37, no. 5, pp. 294–297, 1985.

[65] M. O. Pohl, I. Busnadiego, V. Kufner et al., "SARS-CoV-2 variants reveal features critical for replication in primary human cells," *PLoS Biology*, vol. 19, no. 3, article e3001006, 2021.

[66] S. Chuenkitmongkol, R. Solante, E. Burhan et al., "Expert review on global real-world vaccine effectiveness against SARS-CoV-2," *Expert Review of Vaccines*, vol. 21, no. 9, pp. 1255–1268, 2022.

[67] H. Chemaitelly, H. H. Ayoub, S. AlMukdad et al., "Duration of mRNA vaccine protection against SARS-CoV-2 omicron ba.1 and ba.2 subvariants in Qatar," *Nature Communications*, vol. 13, no. 1, p. 3082, 2022.

[68] H. Ke, M. R. Chang, and W. A. Marasco, "Immune evasion of SARS-CoV-2 omicron subvariants," *Vaccines*, vol. 10, no. 9, p. 1545, 2022.

[69] H. F. Tseng, B. K. Ackerson, K. J. Bruxvoort et al., "Effectiveness of mRNA-1273 vaccination against SARS-CoV-2 omicron subvariants BA.1, BA.2, BA.2.12.1, BA.4, and BA.5," *Nature Communications*, vol. 14, no. 1, p. 189, 2023.

[70] F. R. Menter, "Two-equation eddy-viscosity turbulence models for engineering applications," *AIAA Journal*, vol. 32, no. 8, pp. 1598–1605, 1994.

[71] F. Webner, A. Kohl, D. Schmeling, and C. Wagner, "Aerosol spread in a generic train entrance: comparison between experiment and numerical simulation," *STAB/DGLR Symposium 2022: New Results in Numerical and Experimental Fluid Mechanics XIV*, pp. 590–600, Springer, 2023.